





# Gold nanodoughnut as an outstanding nanoheater for photothermal applications

JAVIER GONZÁLEZ-COLSA,<sup>1</sup>  GUILLERMO SERRERA,<sup>1</sup>  JOSÉ MARÍA SAIZ,<sup>1</sup> DOLORES ORTIZ,<sup>1</sup> FRANCISCO GONZÁLEZ,<sup>1</sup> FERNANDO BRESME,<sup>2</sup> FERNANDO MORENO,<sup>1</sup>  AND PABLO ALBELLA<sup>1,\*</sup> 

<sup>1</sup>Group of Optics, Department of Applied Physics, University of Cantabria, 39005 Santander, Spain

<sup>2</sup>Department of Chemistry, Molecular Sciences Research Hub, Imperial College London, W120BZ London, UK

\*[pablo.albella@unican.es](mailto:pablo.albella@unican.es)

**Abstract:** Photoinduced hyperthermia is a cancer therapy technique that induces death to cancerous cells via heat generated by plasmonic nanoparticles. While previous studies have shown that some nanoparticles can be effective at killing cancer cells under certain conditions, there is still a necessity (or the need) to improve its heating efficiency. In this work, we perform a detailed theoretical study comparing the thermoplasmonic response of the most effective nanoparticle geometries up to now with a doughnut-shaped nanoparticle. We numerically demonstrate that the latter exhibits a superior tunable photothermal response in practical illumination conditions (unpolarized light). Furthermore, we show that nanoparticle heating in fluidic environments, i.e., nanoparticles undergoing Brownian rotations, strongly depends on the particle orientation with respect to the illumination source. We conclude that nanodoughnuts are the best nanoheaters in our set of structures, with an average temperature increment 40% higher than the second best nanoheater (nanodisk). Furthermore, nanodoughnuts feature a weak dependence on orientation, being therefore ideal candidates for photothermal therapy applications. Finally, we present a designing guide, covering a wide range of toroid designs, which can help on its experimental implementation.

Published by Optica Publishing Group under the terms of the [Creative Commons Attribution 4.0 License](https://creativecommons.org/licenses/by/4.0/). Further distribution of this work must maintain attribution to the author(s) and the published article's title, journal citation, and DOI.

## 1. Introduction

Nowadays cancer diseases seriously endanger the public health affecting people worldwide. In fact, it is estimated that around 19.3 million of new cancer cases and 10 million related deaths took place in 2020 [1,2], with a rapidly growing trend in recent times [3,4]. Current medical treatments based on surgical resection, chemotherapy, and radiotherapy present a wide range of negative side effects which often traduces in a quality-of-life reduction. Consequently, these techniques need to be revisited and complemented with other alternatives to constitute a definitive solution [5]. Thus, novel methods with higher effectivity and side effect free are sought.

Among the existing alternative therapies, hyperthermia treatments involve local heating at 42–48°C [6], leading to inhibition of protein activation and DNA synthesis [7,8] inducing cell death, with widely spread approaches like radiofrequency or microwave ablation [9]. However, macroscopic heating methods might affect large tissue areas, resulting potentially in the damage of healthy tissue as well as other side effects [10]. On the other hand, Photothermal Therapy (PTT), using absorbing nanoparticles as microscopic photothermal agents, can focus high temperatures in the region around the cancerous cells, hence preventing the damage of healthy tissue and improving the therapeutic effectivity of heating [11].

The success of the PTT relies strongly on the heating source, i.e., the optically absorbing agent employed. A wide range of materials, including bovine serum albumin heterojunctions [12], graphene nanoparticles and carbon nanotubes [13], are being investigated for PTT applications, but the most widespread and promising PTT agents are based on Localized Surface Plasmon (LSP) resonances in nanoparticles [14]. These nanoparticles allow for local heat generation by resistive losses enhancement caused by light absorption at the plasma eigenfrequency. The plasma eigenfrequency of a particle depends strongly on its composition, shape and size. All these variables can be exploited to produce highly tunable heating agents. Most noble metals exhibit LSP resonances in the UV-VIS-NIR range [15], but gold is the preferred material, due to its biocompatibility, weak cytotoxicity, and low reactivity. Furthermore, gold LSP resonances can be taken to the NIR, close to the so called “biological windows” (700-900 nm, 1000-1400 nm) [16], in which human tissues are dispersive –causing light depolarization– but low absorbing. Therefore, the design of particles with main absorption in this wavelength range is a key objective in PTTs, as they provide optimum heating conditions for the nanoparticles minimizing the non-selective heating of healthy tissues.

LSP resonances of nanoparticles can be controlled both, in magnitude and spectral position, by changing its shape and size. These variables therefore are critical to optimize the PTT performance [17–19]. The rational design of nanoparticles drives many theoretical [20] and experimental efforts [21]. Among the most popular geometries [19], nanorods [22–24], core-shell nanoparticles [25–27] and nanostars [28,29], gold nanorods have attracted significant attention since they can be easily synthesized, producing monodisperse particles with well-defined aspect ratios and sizes below 120 nm [30–33], as nanoparticles should be small enough to penetrate small capillaries and get adsorbed to cells. Spherical gold nanoparticles feature resonances closer to the visible spectrum, but they can be combined into clusters [34,35] that lead to a redshift, and resonances closer to those corresponding to the biological windows. The collective effects can also enhance the performance of isolated nanoparticle thermo-optical responses giving rise to bigger temperatures as reported in [36,37]. Another aspect that has been covered with this type of systems is the impact of nanoscale curvature, which is relevant in small nanoparticles, on the efficiency of heat transfer from the particle to the solution. Recently, it was shown that nanoscale curvature influences the interfacial thermal conductance, resulting in enhanced thermal transport from particle to fluids [38]. The main impact of the thermal conductance is an increase of the nanoparticle temperature relative to the temperature of the particle for an infinite thermal conductance, assumed in our work. However, the thermal conductance does not affect the boundary condition of the fluid at the nanoparticle surface, namely, the surface fluid temperature [39] and will not influence the main conclusions we obtained.

Anisotropic structures provide an ideal approach to tune the spectral thermal response of nanoparticles [40]. However, when these particles diffuse freely in solution, their absorption is strongly dependent on the nanoparticle orientation with respect to the direction of the light source [40,41], affecting significantly their heating performance. Toroidal nanoparticles, whose fabrication in colloid has been recently demonstrated [24,42], have also been explored [43] compared with rods and rings.

In this work, we demonstrate theoretically that doughnut-shaped nanoparticles, as single heaters, outperform the most used PTT agents, offering high spectral tunability, high performance of light into heat conversion and weak dependence of heating on orientation in solution. With this purpose we perform an exhaustive theoretical comparison of the spectral photothermal response of the most relevant gold nanostructures with a doughnut-shaped nanoparticle. Finally, a guide to design nanodoughnuts with tunable heating properties is provided.

## 2. Methods and theoretical background

One of the most efficient ways to understand photothermal effects in plasmonic nanoparticles was introduced by Govorov et al. [44]. The heat equation for a single spherical nanoparticle was solved and the steady state temperature as a function of the radial distance  $r$  can be derived analytically, with the well-known expression

$$\Delta T(r) = \frac{V_{NP}Q}{4\pi k_0 r} \quad (1)$$

where  $V_{NP}$  is the nanoparticle volume,  $r > R_{NP}$  is the radial distance,  $R_{NP}$  is the nanoparticle radius and  $k_0$  is the thermal conductivity of the surrounding medium. Here, the heat losses  $Q$  in the particle can be obtained by means of the Joule effect expression

$$Q(\vec{r}) = \langle \vec{J}(\vec{r}, t) \cdot \vec{E}(\vec{r}, t) \rangle \quad (2)$$

where  $\vec{E}$  is the electric field inside the sphere,  $\vec{J}$  is the current density,  $\vec{r}$  is the position vector, and  $t$  is the time. In most cases, intricate nanoparticle geometries prevent an analytical solution of the scattering problem in the nanoparticle. However, for a spherical nanoparticle, the electric field inside the sphere can be obtained by means of the quasi-static approximation [45], where the sphere size is much smaller than the excitation wavelength. Under this approximation, the  $Q$  value can be obtained as

$$Q = \frac{\omega}{8\pi} E_0^2 \left| \frac{3\epsilon_0}{2\epsilon_0 + \epsilon_{NP}} \right|^2 \Im m[\epsilon_{NP}] \quad (3)$$

where  $\omega$  is the angular frequency,  $E_0$  the electric field amplitude,  $\epsilon_0$  is the surrounding medium permittivity and  $\epsilon_{NP}$  the permittivity of the nanoparticle. This model is a useful initial tool to qualitatively understand the heating processes in nanoparticles.

In general, metal nanoparticles (disregarding their geometry) can efficiently generate heat under optical excitation, especially around the plasmonic resonance wavelength which depends on the material, shape and size (as can be seen in Eq. (3)). The heat generation process involves not only absorption of incident photons, but also the heat transfer from the nanoparticle to the surrounding medium. A very simple mechanism takes place: the incident electric field strongly drives mobile carriers of the metal, heating the material owing to the energy gained by these carriers. Then, heat diffuses away from the nanostructure and leads to a temperature increase of the surrounding medium. In the absence of phase transformations, the temperature distribution around optically stimulated nanoparticles can be described by the usual heat transfer equation:

$$\rho(\mathbf{r})c(\mathbf{r})\frac{\partial T(\mathbf{r}, t)}{\partial t} = \nabla k(\mathbf{r})\nabla T(\mathbf{r}, t) + Q(\mathbf{r}, t) \quad (4)$$

where  $r$  and  $t$  are the position and time,  $T(r, t)$  is the local temperature and the material parameters  $\rho(r)$ ,  $c(r)$  and  $k(r)$  are the mass density, specific heat and thermal conductivity, respectively. The function  $Q(r, t)$  represents the energy (heat) source coming from light dissipation (electromagnetic losses). The solution of this equation has a transient state, and after a characteristic time, it reaches its steady state. Thermal processes in metals are fast, which means that a steady state is rapidly reached for typical incident powers and metal nanoparticle dimensions, like those used in nanomedicine. To obtain the electromagnetic losses, the system of Maxwell's equations including appropriate boundary conditions must be written, which in the case of complex topologies, such as core-shell or stars geometries, must be solved numerically.

In our case, the whole process of light absorption and subsequent heat transfer between the nanostructure and the surrounding medium has been modelled by means of finite element simulations. For an easy implementation and reliability of the solution, we have chosen Comsol Multiphysics 5.6, a software that provides state-of-the-art routines to solve partial differential

equations. In our simulations, we have assumed that particles are illuminated with circularly polarized light to emulate the more realistic unpolarized illumination. Unpolarized light can be simulated by just solving the problem for two orthogonal input electric fields, but this doubles the simulation time. Thus, circular polarization gives equivalent results while being computationally more efficient (see [Supplement 1](#), Fig. S1 for an extended discussion). As usual [20,46,47], the numerical solution of thermoplasmonic problems can be found with finite element methods (FEM). This is done in two steps, the first consists in solving the electromagnetic part of the problem to obtain the resistive losses distribution (heat source). This is done by finding the solution of the Maxwell equations with the RF Comsol Module. A free tetrahedral mesh with element sizes controlled by the excitation wavelength was used to guarantee a high element density and quality, and reliable curvatures when needed. The second step involves the calculation of the spectral and spatial temperature distribution. This requires a Heat Transfer Module that uses the ohmic losses found in the first step as input. To consider heat dissipation in our simulation region, we used a heat flux node across the outer boundaries, considering a heat transfer coefficient, dependent on the geometry and the ambient flow conditions. The heat transfer coefficient  $h$  can often be estimated by dividing the thermal conductivity of the fluid by a length scale. All the thermal parameters involved in our calculations (density, specific heat and thermal conductivity) were taken from the Comsol Multiphysics material database.

### 3. Results and discussion

#### 3.1. Geometry comparison

Most experiments aimed at photoinduced hyperthermia consider a setup like the one illustrated in Fig. 1(a), where metallic nanoparticles flowing in a capillary generate local heat by excitation of LSP resonances when illuminated with a laser beam. The nanoparticles feature free rotational diffusion and therefore adopt all orientations with the same probability for the case of isotropic nanoparticles (see Fig. 1), highlighting the importance of considering the spectral thermal response of the nanoparticles for different orientations with respect to the light source. In the specific case of phototherapy against cancer, the temperature of the sample (either in vivo or in vitro) needs to reach temperatures between 42-48 degrees Celsius [48], namely, about 10 degrees above the average temperature of the biological medium, for the conditions and thermo-optical properties of the human tissue. However, it is necessary to exert a dynamic control of the temperature increases to avoid uncontrollable damage of the healthy surrounding tissue, as it would happen with continuous wave lasers. Pulsed lasers are widely used to avoid these issues, because tissues can suffer different processes such as photochemical damage, photothermal damage, photoablation or photo disruption as a function of the power density and the exposure time [49]. Thus, sudden and high thermal responses are desired at power densities as lower as possible. For photothermal therapies, this is achievable by considering more efficient nanoparticles in terms of light/heat conversion.

A thorough theoretical comparison of the photothermal spectral response of different particle shapes was performed. Electromagnetic and thermal simulations were carried out under plane wave VIS-NIR illumination unpolarized light, since as the light beam travels through tissues, multiple absorption and scattering phenomena take place, unpolarizing it partially.

The geometries considered for this comparison are shown in Fig. 1 and include some of the most widely used shapes: spheres, spherical gold/silica core-shells, nanostars, disks, rectangular rods (similar results to rounded rods as shown in [Supplement 1](#), Fig. S2) and toroids. All particles have been designed considering a therapeutically allowed maximum dimension size of 120 nm and compared under the same conditions selecting the best design in terms of its potential heating capability. The particle designs are sought to provide the highest possible temperature for a given intensity. This would allow the nanostructures to generate heat efficiently even with minor incident power which is essential in photothermal therapy applications where human tissues

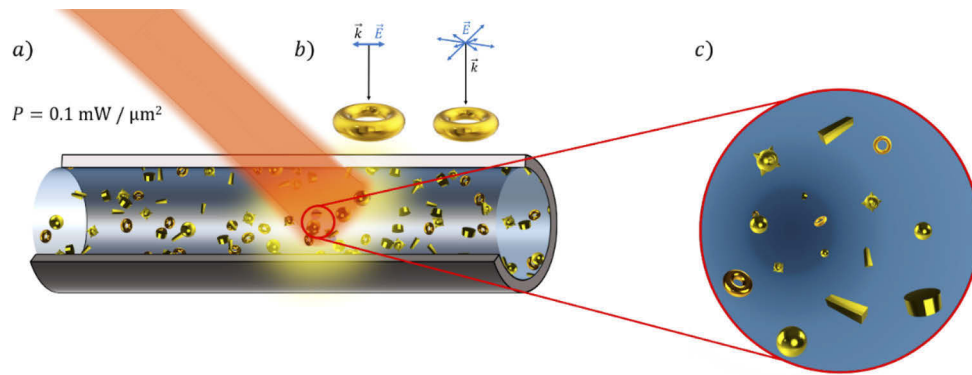


**Fig. 1.** Standard thermofluidic application of this work. a) Studied nanoparticle shapes inside a fluidic channel. b) Illumination process of the system. c) Randomly oriented particle. Upon excitation by light, the effective temperature increase will correspond to the average temperature achieved by all possible orientations.

induce an exponential decay of the light intensity [50]. Following previous studies [51,52], we consider the analytical solution of the classical heat equation for an initial theoretical analysis of the heating effects. A very good agreement between theory and simulation can be observed for spherical particles below 30 nm in radius. However, deviations are observed for larger particles in the regime where the particle size is not sufficiently small to fulfil the quasi-static approximation considered in Eq. (1). In this regime, the particle is influenced by a time dependent electric field which translates into a non-uniform electronic density motion, thus, reducing the magnitude of the resistive losses and consequently the electromagnetic absorption (see Supplement 1, Figs. S3 and S4 for a systematic sizes study of both, electromagnetic absorption and temperature increment, respectively).

Fig. 2 shows the photothermal spectral response of the complete set of nanoparticle shapes considering its steady (Fig. 2(a)) and time dependent thermal response (Fig. 2(b)) calculated in aqueous environment, irradiated at normal incidence for both, linearly polarized and unpolarized light with an intensity of  $0.1 \text{ mW}/\mu\text{m}^2$ , several orders of magnitude smaller than those considered in previous works [43,47,53] (see Supplement 1, Fig. S5 for other excitation power densities). All particle shapes were optimized by changing the geometrical parameters of each shape (within a maximum dimension size of 120 nm) and selecting those that yield the greatest temperature increment. The optimal dimensions for each geometry offer a better thermal performance compared with other configurations of the same volume for the same structure (see Fig. S6 in Supplement 1). We then compare the photothermal behavior, focusing on the pros and cons that each shape offers. A detailed physical discussion of the different responses can be found in Supplement 1.

In Fig. 2(a), it can be seen that the disk, rod and toroid clearly outperform the sphere, core-shell and star shapes in terms of maximum temperature increase. Although the sphere is the most widely used geometry in biomedical applications (PTT, drug delivery, microfluidics, gene therapy and imaging, for instance) [54,55], partly due to the simplicity of fabrication, it shows a poor thermal response in comparison with other geometries. It displays a maximum temperature increment of  $\Delta T \approx 6 \text{ K}$ , at a wavelength far from the biological windows, offering negligible tunability compared to the rest of the analyzed structures [56] and limiting its applicability to clusters, where collective effects play a definitive role. Meanwhile, the gold/silica core-shell although located closer to the more usable wavelengths of the first biological window (700-900 nm [15]), still shows a low temperature increase  $\Delta T \approx 7 \text{ K}$  in contrast to the upper three shapes and shows subpar tunability [33], allowing its use only in the first and less beneficial window at



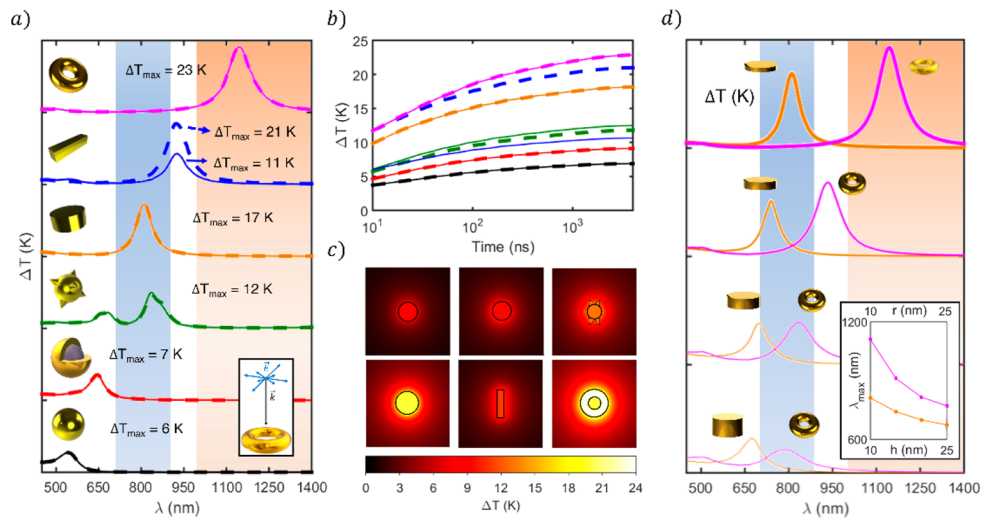


**Fig. 2.** Thermal response of the compared gold nanoparticle shapes in water for linearly polarized (dotted line) and unpolarized (continuous line) light at normal incidence. The sphere (in black) has a radius of 40 nm, core-shell (in red) has a core radius of 30 nm and a shell thickness of 10 nm. The core of stars (in green) has a radius of 30 nm with a cone height of 30 nm. The disk (in orange) radius is 50 nm, with a height of 10 nm. The dimensions of the rectangular rod (in blue) are  $30 \times 120 \times 30$  nm. Finally, the doughnut or toroid shape (in pink) has a main radius of 50 nm and a secondary radius of 10 nm. a) Optimal thermal response for each analyzed geometry considering a major dimension lower than 120 nm are plotted for temperatures between 0 and 25 K. The blue and reddish shadowed regions represent the first and second biological windows, respectively. b) Transient optimal point heating for the shapes shown in a). c) Maximum temperature increases spatial distribution for each geometry. d) Tunability comparison of disks and toroids between 0 and 25 K. The disk radius is fixed at 50 nm and the torus main radius at 50 nm. The disk heights are 10, 15, 20 and 25 nm and the torus secondary radii, 10, 15, 20 and 25 nm. Relative wavelength displacement is plotted in the inset.

the price of lower temperature increments (see Figs. S7 and S8 in [Supplement 1](#)). Finally, the nanostar geometry shows a similar behavior to the core-shell, with a mild temperature increment around 12 K at the same excitation wavelengths. However, its response is extremely sensitive to the height of the cones and show a substantial dependance with their number. Hence, its fabrication is crucial and challenging to reach the desired photothermal response.

On the other hand, the disk, rod and toroidal shapes show better thermal response in all aspects (magnitude, spectral tunability and response time). The disk shows a better performance in terms of heating however the optimal geometry requires an especially thin height of 10 nm with a radius of 50 nm to achieve the maximum temperature, resulting in a challenging fabrication process [57]. In the case of the nanorod, its thermal response displays a redshift with respect to the disk. Furthermore, a huge discrepancy between linearly polarized and unpolarized light responses exists. A linear polarization illumination (input electric field polarized along the greatest dimension of the rod) gives a temperature increment peak of 21 K, higher than the observed for the disk. However, for unpolarized light, a considerable reduction in the temperature increment can be observed, resulting in a lower maximum temperature increment of around 11 K, closer to the core-shell response.

This polarization dependence is a clear disadvantage in the performance of the rod against other particles, as the light beam usually becomes unpolarized when traveling through tissues, due to

the multiple absorption and scattering phenomena. Finally, the last considered shape to improve thermal response in nanoparticles is a toroidal geometry, which offer the best performance, with an outstanding increment in maximum temperature increment of around 23 K, a 35% of increase (see [Supplement 1](#), Fig. S9 for temperature increments in other surrounding media) when compared with the second largest temperature increment in unpolarized illumination (17 K for the disk). As we will demonstrate later, the toroid also shows the greatest tolerance to rotations with respect to the incident beam, which guarantees a reliable performance in thermofluidic and photothermal therapy applications.

Fig. 2(b) shows the results of the thermal time-dependent calculations at the optimal wavelengths depicted in Fig. 2(a). It can be seen that the three worst particles require also longer times to reach the steady state (considered to be when 90% of the maximum temperature increment is reached, see [Supplement 1](#), Fig. S10 for further discussion), up to around 320 ns for the sphere and core-shell, the star having a larger time of 330 ns. In contrast, the three best heating candidates' shapes reach the steady state faster, with times more than 20% shorter (260 ns for disks and rods), furthering the case of those three nanoparticles. Furthermore, the toroidal particle also reaches its maximum temperature after a 300 ns illumination, being one of the three fastest heaters. This can be explained in terms of volume. As the optimal rods, disks and toroids have smaller volumes, they reach the steady state in a shorter time. A clear way to summarize the thermal behavior of all studied shapes, is to consider its temperature spatial distribution (Fig. 2(c)). Disks and toroidal particles offer very high temperatures for unpolarized light and heat up the greatest surrounding region, while the rest of geometries show much lower heating capacity. Toroids also show high temperatures in the water region confined in the inner hole, while all geometries display their maximum temperature inside gold.

Another key feature when bringing these different heaters to practical applications is their spectral tunability, which has been investigated through variation of the geometrical parameters (see [Supplement 1](#), Figs. S11–S19 for further information). This has been compared in Fig. 2(d) for disks and toroids. Starting from two designs that offer comparable thermal responses, the characteristic parameters (height for the disk and secondary radius for toroids) have been varied keeping the main radius constant for both geometries. It can be seen how for equivalent geometrical variations, we can get larger wavelength shifts. Moreover, in the case of the disk it is impossible to bring its thermal response to the second biological window (see inset of Fig. 2(d)). This clearly demonstrates the significantly better tunability of toroidal shaped nanoparticles. The comparison shown in Fig. 2, evidences the photothermal response superiority of the rod, disk and toroidal geometries, showing the last one a better response in magnitude and spectral tunability (see [Supplement 1](#), Fig. S20 to visualize the corresponding study in air).

### 3.2. Nanoparticle orientation dependance

Another important aspect in photothermal applications, is the fact that the heating response of nanoparticles in a fluid strongly depends on the particle orientation with respect to the illumination source. Since nanoheaters will rotate freely around the fluid, the effective temperature obtained upon illumination will correspond to the average of the temperatures achieved by all possible orientations. Thus, particles with small thermal dependence to the incident beam - structure relative orientation will offer better effective performance. This aspect was considered in a previous theoretical work [43], under linearly polarized excitation, showing the absorption cross section for rods and toroids. In this work, we provide the angular average temperature value, appropriate to compare the heating performance, that the aforementioned nanoheater candidates can reach.

To clearly discern which of the three best heaters (rod, disk and toroid) stands out and why, we considered the three of them immersed in water and calculated how their relative orientation to the exciting light affects their thermal response. Fig. 3 shows the temperature maps of unpolarized

light excited nanoparticles for all possible 3D rotations with respect to the  $x$  and  $y$  axes, taking their optimal response orientation as the initial position (see Supplement 1, Fig. S21 for a similar study in air). These rotations, seen as points on the unit sphere, are represented by  $\theta$  and  $\phi$  for the  $x$  and  $y$  axes respectively, as shown in the illustration of Fig. 3(a). To extract the angular average temperature, we use a set of rotations equally distributed on the sphere surface, leading to a uniformly sparse set of points. This consideration is required to guarantee that all rotations are equiprobable and all points equally weighted.

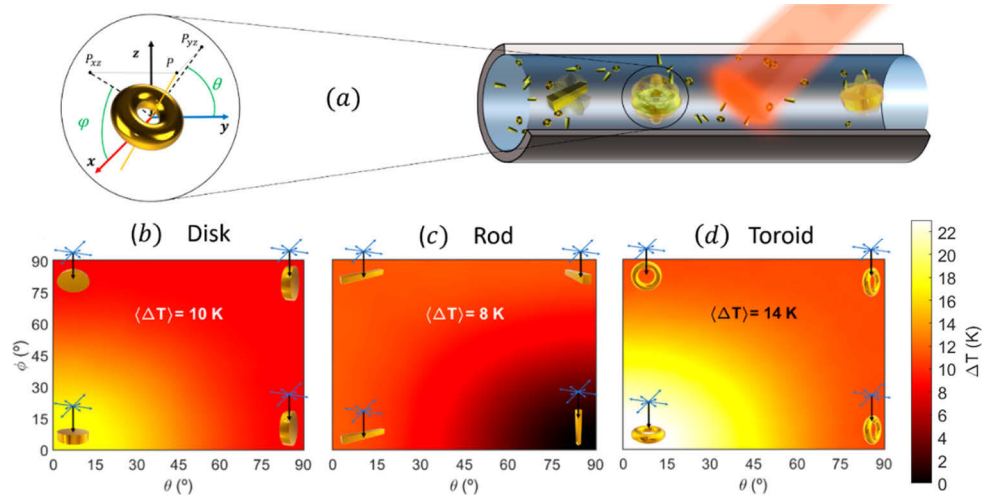


**Fig. 3.** Thermal responses of the three best nanoheaters in Fig. 2 to rotations. a) Illumination and rotation outline.  $\theta$  and  $\phi$  are the rotations with respect to the  $x$  and  $y$  axes and the considered power density is  $0.1\text{ mW}/\mu\text{m}^2$ . Maximum temperature increases for unpolarized light as a function of rotation angles: b) Disk; c) Rod; d) Toroid. The average temperature is shown for all cases.

Looking at the disk results in Fig. 3(b), it can be seen how the temperature distribution shows a revolution symmetry in the colormap, as the revolution axis of the disk and the  $z$  axis (beam direction) match in the initial configuration. Thus, considering the temporal evolution of the electric field vector, rotating the disk about the  $y$  axis, and subsequently about the  $x$  axis, has the same effect as rotating it about the  $x$  axis and then about the  $y$  axis. To facilitate the understanding of this figure, setting  $\theta = 0^\circ$  and then increasing the rotation in  $\phi$  will mean that eventually the transverse length and the electric field will be eventually parallel, so that occasional resonances will be produced, resulting in a decrease in the mean value of the temperature increment of around 41% compared to the most favorable configuration ( $\Delta T = 17\text{ K}$ ). Thus, due to its symmetry, the disk exhibits a reasonably stable thermal response to rotation.

In Fig. 3(c) (rod), an obvious symmetry in the angular distribution of the temperature increment can be observed. At  $\theta = 0^\circ$ , the major axis of the rod is orthogonal to the beam wavevector, and therefore the rotating electric field will occasionally align with this direction for any  $\phi$  value, guaranteeing a constant thermal response. However, setting  $\theta = 90^\circ$  and  $\phi = 0^\circ$ , the major axis is orthogonal to the electric field at any time, preventing favorable resonances and heating. In this case, as  $\phi$  grows, the projection of the aforementioned major axis along the direction of the electric field vector increases, promoting enhancement of the thermal response. Fig. 3(c) clearly shows that the rod displays a worse temperature angular distribution than the disk. Thus, the angular average temperature increment is significantly smaller (8 K), translating in a reduction of 62% with respect to the maximum achievable value ( $\Delta T = 21\text{ K}$ ). This is due to the fact that the



electric field is oscillating in time, reducing the efficiency of the generated mode in the rod and consequently its thermal response.

The case of the toroidal particle, shown for the same angle configuration in Fig. 3(d), exhibits weaker variations in the increase of temperature for any  $\phi$  value upon rotation in  $\theta$ . A reduction of temperature increments is observed symmetrically for rotations in  $\phi$  and  $\theta$ , achieving a stable value of around 12 K for a full  $90^\circ$  rotation in either  $\phi$  or  $\theta$ . As in the case of the disk, as the electric field vector rotates over time, there always exists a configuration in which this vector is parallel to the toroid transversal length, allowing a continuous excitation of the corresponding mode. However, for each time in which the previous situation occurs, the opposite also takes place, with the electric field vector orthogonal to the toroid transversal length, avoiding the possible excitation mode. This leads to a compromise between both configurations, giving rise to a less time dependent excitation. The average temperature increment results in a reduction of 39% with respect to the most favorable configuration ( $\Delta T = 23$  K), proving that toroidal nanoparticles have a high tolerance to rotations and providing the highest angular average temperature increment compared to disks and rods.

### 3.3. Optimal spectral photothermal response: a guide for toroidal particle design

We have shown that toroidal particles offer the best nanoheating performance in our set of geometries, with minimal loss due to rotational diffusion. Here, we perform now, an exhaustive analysis of the dependence of the temperature increase with the geometrical features of this nanoparticle. This investigation provides a clear and direct theoretical guide to select the working spectrum and the specific dimensions of the torus depending on the considered application.

Fig. 4 shows two color maps that correspond to the temperature increment produced by the toroid immersed in water (Fig. 4(a)) and the wavelength at which the optimal resonance occurs for each case (Fig. 4(b)). The corresponding study in air is shown in Supplement 1, Fig. S22. As in the previous cases, possible phase changes in the gold nanoparticles have not been considered since most applications involve an aqueous medium in which the maximum temperature increments are lower than 30 K for the considered power density. According to the

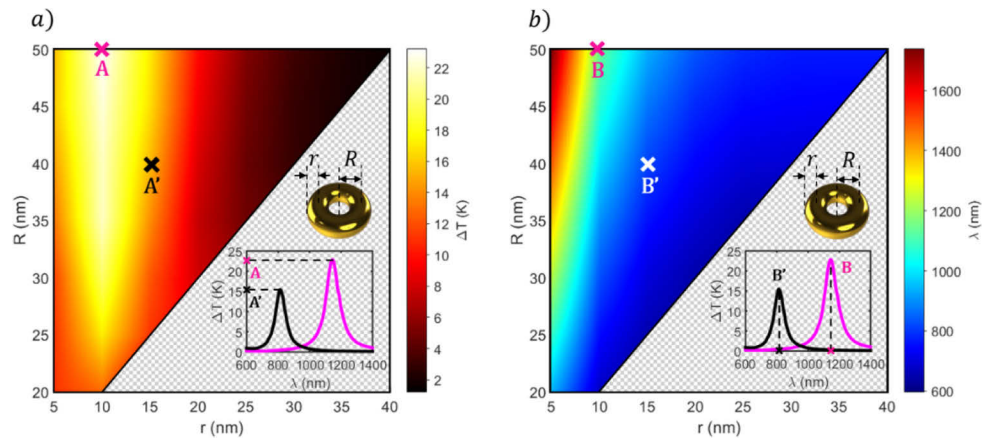


**Fig. 4.** Thermal response of a fully tuned toroidal nanoparticle. a) Maximum temperature increases of toroid for main ( $R$ ) and secondary ( $r$ ) radius variations represented between 0 and 25 K. b) Corresponding excitation wavelength of the maximum thermal response as a function of the main and secondary radii. The points A and B correspond to the spectral maximum temperature increase (inset) for the toroid shown in Fig. 2,  $R = 50$  nm and  $r = 10$  nm. The points A' and B' correspond to other spectral maximum temperature increase for the  $R = 40$  nm and  $r = 15$  nm toroid.

aforementioned maximum size (120 nm), main radii lower than 50 nm have been examined. In addition, a secondary radius larger than 5 nm has been assumed. Below that value calculations become very speculative, because the deposition of metallic materials with these thicknesses is a huge manufacturing challenge, and the shape/size precision cannot be guaranteed [58,59].

The dependence of both parameters, temperature increase and excitation wavelength, with the dimensions of the nanodoughnut is directly related and follows the same pattern. Notice that the maximum increment of temperature is reached only when fixing the secondary radius around 10 nm. As we increase that parameter, the toroidal geometry gets closer to a sphere, and so does the increase in temperature. On the other hand, secondary radii smaller than 10 nm would lead to a reduced toroid cross section, hindering the support of strong electromagnetic modes that can produce high thermal responses. An opposite behavior appears when looking at the main radius, showing in general a growth of temperature increment for larger values. This can be explained in terms of the excited mode in the geometry. As the main radius increases, the toroid length grows shifting the excited mode towards longer wavelengths and enhancing the corresponding resistive losses.

#### 4. Conclusions

We have performed a numerical investigation of the photothermal response of different gold nanostructures, demonstrating that the nanodoughnut shape displays an optimum performance with a temperature increment about 40% higher than the second-best heater shape, the nanodisk. The doughnut shape outclasses the temperature increments of the most widely used nanostructures, offering the largest heating areas, and also showing superior spectral tunability, supporting strong resonances within the therapeutic windows and particle sizes considering the recommended therapeutical limits for biomedical applications. We have also analyzed, the impact of nanoparticle rotational diffusion on its photothermal performance. The nano-doughnut shape features the highest average temperature increment and shows a high tolerance to rotation compared to other structures. For these reasons, it is foreseen as ideal candidate for photothermal applications. Finally, in view of the advantages offered by the toroidal shape, a simple and practical guide that can facilitate its design to act as an efficient heater in a desired spectral range has been provided.

We believe that the results and conclusions of this work highlight the promise of improving customized cancer treatments in a near future. This investigation could also help researchers to optimize the thermal performance of other fluidic systems, such as those using phase changing material heating, wettability or oil heating. Although in this study the maximum dimension has been limited to 120 nm following the most common recommendations in biomedical applications, Fig. 4 suggests that larger nanodoughnuts can also be exceptional candidates in other spectral regions out of the biological windows, making them available for other applications. Thus, our investigation, although focused on biological applications, could be extended to other areas that may need a careful selection of the nanoheater material and its consequent spectral photothermal optimization.

**Funding.** Ministerio de Economía y Competitividad (PGC2018-096649-B-I, RYC-2016-20831); Leverhulme Trust (RPG-2018-384); Engineering and Physical Sciences Research Council (EP/J003859/1).

**Acknowledgments.** Authors would like to thank A. Franco and C. R. Crick for the interesting discussions. We gratefully acknowledge financial support from Spanish national project (No. PGC2018-096649-B-I), the UK Leverhulme Trust (Grant No. RPG-2018-384), UK-EPSC (EP/J003859/1) and Imperial College Europeans Partner Fund grant. J. G-C. thanks the Ministry of science of Spain for his FPI grant. G. S. thanks the Ministry of education for his collaboration grant and P.A. acknowledges funding for a Ramon y Cajal Fellowship (Grant No. RYC-2016-20831).

**Disclosures.** The authors declare no conflict of interest.

**Data availability.** No data were generated or analyzed in the presented research.

**Supplemental document.** See [Supplement 1](#) for supporting content.

## References

1. H. Sung, J. Ferlay, R. L. Siegel, M. Laversanne, I. Soerjomataram, A. Jemal, and F. Bray, "Global Cancer Statistics 2020: GLOBOCAN Estimates of Incidence and Mortality Worldwide for 36 Cancers in 185 Countries," *CA A Cancer J Clin* **71**(3), 209–249 (2021).
2. R. L. Siegel, K. D. Miller, and A. Jemal, "Cancer statistics, 2019," *CA A Cancer J Clin* **69**(1), 7–34 (2019).
3. B. Vogelstein, N. Papadopoulos, V. E. Velculescu, S. Zhou, L. A. Diaz, and K. W. Kinzler, "Cancer genome landscapes," *Science* **340**(6127), 1546–1558 (2013).
4. D. M. Parkin, F. I. Bray, and S. S. Devesa, "Cancer burden in the year 2000. The global picture," *Eur. J. Cancer* **37**(SUPPL. 8), 4–66 (2001).
5. P. Gotwals, S. Cameron, D. Cipolletta, V. Cremasco, A. Crystal, B. Hewes, B. Mueller, S. Quarantino, C. Sabatos-Peyton, L. Petruzzelli, J. A. Engelman, and G. Dranoff, "Prospects for combining targeted and conventional cancer therapy with immunotherapy," *Nat. Rev. Cancer* **17**(5), 286–301 (2017).
6. K. F. Chu and D. E. Dupuy, "Thermal ablation of tumours: Biological mechanisms and advances in therapy," *Nat. Rev. Cancer* **14**(3), 199–208 (2014).
7. X. Ma, Y. Wang, X. L. Liu, H. Ma, G. Li, Y. Li, F. Gao, M. Peng, H. M. Fan, and X. J. Liang, "Fe<sub>3</sub>O<sub>4</sub>-Pd Janus nanoparticles with amplified dual-mode hyperthermia and enhanced ROS generation for breast cancer treatment," *Nanoscale Horiz.* **4**(6), 1450–1459 (2019).
8. D. R. Canci, D. Paschek, and A. E. Garcia, "Equilibrium study of protein denaturation by urea," *J. Am. Chem. Soc.* **132**(7), 2338–2344 (2010).
9. X. Zhu, W. Feng, J. Chang, Y. W. Tan, J. Li, M. Chen, Y. Sun, and F. Li, "Temperature-feedback upconversion nanocomposite for accurate photothermal therapy at facile temperature," *Nat. Commun.* **7**, 10437 (2016).
10. M. C. Jansen, F. H. Van Duijnhoven, R. Van Hillegersberg, A. Rijken, F. Van Coevorden, J. Van Der Sijp, W. Prevoo, and T. M. Van Gulik, "Adverse effects of radiofrequency ablation of liver tumours in the Netherlands," *Br. J. Surg.* **92**(10), 1248–1254 (2005).
11. L. R. Hirsch, R. J. Stafford, J. A. Bankson, S. R. Sershen, B. Rivera, R. E. Price, J. D. Hazle, N. J. Halas, and J. L. West, "Nanoshell-mediated near-infrared thermal therapy of tumors under magnetic resonance guidance," *Proc. Natl. Acad. Sci. U. S. A.* **100**(23), 13549–13554 (2003).
12. Z. Guo, S. Zhu, Y. Yong, X. Zhang, X. Dong, J. Du, J. Xie, Q. Wang, Z. Gu, and Y. Zhao, "Synthesis of BSA-Coated BiOI@Bi<sub>2</sub>S<sub>3</sub> Semiconductor Heterojunction Nanoparticles and Their Applications for Radio/Photodynamic/Photothermal Synergistic Therapy of Tumor," *Adv. Mater.* **29**(44), 1–12 (2017).
13. Z. M. Markovic, L. M. Harhaji-Trajkovic, B. M. Todorovic-Markovic, D. P. Kepić, K. M. Arsić, S. P. Jovanović, A. C. Pantovic, M. D. Dramićanin, and V. S. Trajkovic, "In vitro comparison of the photothermal anticancer activity of graphene nanoparticles and carbon nanotubes," *Biomaterials* **32**(4), 1121–1129 (2011).
14. M. Chang, Z. Hou, M. Wang, C. Li, and J. Lin, "Recent Advances in Hyperthermia Therapy-Based Synergistic Immunotherapy," *Adv. Mater.* **33**(4), 1–29 (2021).
15. G. Baffou, *Thermoplasmonics* (Cambridge University, 2018).
16. E. Hemmer, A. Benayas, F. L  gar  , and F. Vetrone, "Exploiting the biological windows: Current perspectives on fluorescent bioprobes emitting above 1000 nm," *Nanoscale Horiz.* **1**(3), 168–184 (2016).
17. G. Baffou, F. Cichos, and R. Quidant, "Applications and challenges of thermoplasmonics," *Nat. Mater.* **19**(9), 946–958 (2020).
18. D. Jaque, L. Mart  nez Maestro, B. Del Rosal, P. Haro-Gonzalez, A. Benayas, J. L. Plaza, E. Mart  n Rodr  guez, and J. Garc  a Sol  , "Nanoparticles for photothermal therapies," *Nanoscale* **6**(16), 9494–9530 (2014).
19. L. Jauffred, A. Samadi, H. Klingberg, P. M. Bendix, and L. B. Oddershede, "Plasmonic Heating of Nanostructures," *Chem. Rev.* **119**(13), 8087–8130 (2019).
20. L. Khosravi Khorashad, L. V. Besteiro, Z. Wang, J. Valentine, and A. O. Govorov, "Localization of Excess Temperature Using Plasmonic Hot Spots in Metal Nanostructures: Combining Nano-Optical Antennas with the Fano Effect," *J. Phys. Chem. C* **120**(24), 13215–13226 (2016).
21. L. Liz-marz, *Colloidal Synthesis of Plasmonic Nanometals* (Jenny Stanford Publishing, 2020).
22. J. Morales-Dalmau, C. Vilches, I. De Miguel, V. Sanz, and R. Quidant, "Optimum morphology of gold nanorods for light-induced hyperthermia," *Nanoscale* **10**(5), 2632–2638 (2018).
23. Y. Wang, K. C. L. Black, H. Luehmann, W. Li, Y. Zhang, X. Cai, D. Wan, S. Y. Liu, M. Li, P. Kim, Z. Y. Li, L. V. Wang, Y. Liu, and Y. Xia, "Comparison study of gold nanohexapods, nanorods, and nanocages for photothermal cancer treatment," *ACS Nano* **7**(3), 2068–2077 (2013).
24. Y. Yan, P. Padmanabha Pillai, J. V. I. Timonen, F. S. Emami, A. Vahid, and B. A. Grzybowski, "Synthesis of toroidal gold nanoparticles assisted by soft templates," *Langmuir* **30**(33), 9886–9890 (2014).
25. C. Ayala-Orozco, C. Urban, M. W. Knight, A. S. Urban, O. Neumann, S. W. Bishnoi, S. Mukherjee, A. M. Goodman, H. Charron, T. Mitchell, M. Shea, R. Roy, S. Nanda, R. Schiff, N. J. Halas, and A. Joshi, "Au nanomatryoshkas as efficient near-infrared photothermal transducers for cancer treatment: Benchmarking against nanoshells," *ACS Nano* **8**(6), 6372–6381 (2014).
26. D. P. O'Neal, L. R. Hirsch, N. J. Halas, J. D. Payne, and J. L. West, "Photo-thermal tumor ablation in mice using near infrared-absorbing nanoparticles," *Cancer Lett.* **209**(2), 171–176 (2004).
27. A. R. Rastinehad, H. Anastos, E. Wajswol, J. S. Winoker, J. P. Sfakianos, S. K. Doppalapudi, M. R. Carrick, C. J. Knauer, B. Taouli, S. C. Lewis, A. K. Tewari, J. A. Schwartz, S. E. Canfield, A. K. George, J. L. West, and N. J.

- Halas, "Gold nanoshell-localized photothermal ablation of prostate tumors in a clinical pilot device study," *Proc. Natl. Acad. Sci. U. S. A.* **116**(37), 18590–18596 (2019).
28. P. Senthil Kumar, I. Pastoriza-Santos, B. Rodríguez-González, F. Javier García De Abajo, and L. M. Liz-Marzán, "High-yield synthesis and optical response of gold nanostars," *Nanotechnology* **19**(1), 015606 (2008).
  29. R. Rodríguez-Oliveros and J. A. Sánchez-Gil, "Gold nanostars as thermoplasmonic nanoparticles for optical heating," *Opt. Express* **20**(1), 621 (2012).
  30. S. Kessentini and D. Barchiesi, "Quantitative comparison of optimized nanorods, nanoshells and hollow nanospheres for photothermal therapy," *Biomed. Opt. Express* **3**(3), 590 (2012).
  31. C. R. Patra, R. Bhattacharya, D. Mukhopadhyay, and P. Mukherjee, "Fabrication of gold nanoparticles for targeted therapy in pancreatic cancer," *Advanced Drug Delivery Reviews* **62**(3), 346–361 (2010).
  32. A. Oyelere, "Gold nanoparticles: From nanomedicine to nanosensing," *NSA* **1**, 45–66 (2008).
  33. N. J. Halas, S. Lal, W. S. Chang, S. Link, and P. Nordlander, "Plasmons in strongly coupled metallic nanostructures," *Chem. Rev.* **111**(6), 3913–3961 (2011).
  34. G. Baffou, R. Quidant, and F. J. García De Abajo, "Nanoscale control of optical heating in complex plasmonic systems," *ACS Nano* **4**(2), 709–716 (2010).
  35. G. Baffou, P. Berto, E. Bermúdez Ureña, R. Quidant, S. Monneret, J. Polleux, and H. Rigneault, "Photoinduced heating of nanoparticle arrays," *ACS Nano* **7**(8), 6478–6488 (2013).
  36. E. Cortés, L. V. Besteiro, A. Alabastri, A. Baldi, G. Tagliabue, A. Demetriadou, and P. Narang, "Challenges in Plasmonic Catalysis," *ACS Nano* **14**(12), 16202–16219 (2020).
  37. A. T. Roberts, J. Yang, M. E. Reish, A. Alabastri, N. J. Halas, P. Nordlander, and H. O. Everitt, "Plasmonic nanoparticle-based epoxy photocuring: A deeper look," *Mater. Today* **27**(August), 14–20 (2019).
  38. A. S. Tascini, J. Armstrong, E. Chiavazzo, M. Fasano, P. Asinari, and F. Bresme, "Thermal transport across nanoparticle-fluid interfaces: The interplay of interfacial curvature and nanoparticle-fluid interactions," *Phys. Chem. Chem. Phys.* **19**(4), 3244–3253 (2017).
  39. K. Metwally, S. Mensah, and G. Baffou, "Fluence Threshold for Photothermal Bubble Generation Using Plasmonic Nanoparticles," *J. Phys. Chem. C* **119**(51), 28586–28596 (2015).
  40. G. Baffou, R. Quidant, and C. Girard, "Heat generation in plasmonic nanostructures: Influence of morphology," *Appl. Phys. Lett.* **94**(15), 1–4 (2009).
  41. M. A. MacKey, M. R. K. Ali, L. A. Austin, R. D. Near, and M. A. El-Sayed, "The most effective gold nanorod size for plasmonic photothermal therapy: Theory and in vitro experiments," *J. Phys. Chem. B* **118**(5), 1319–1326 (2014).
  42. T. H. Chow, Y. Lai, X. Cui, W. Lu, X. Zhuo, and J. Wang, "Colloidal Gold Nanorings and Their Plasmon Coupling with Gold Nanospheres," *Small* **15**(35), 1–12 (2019).
  43. F. Alali, I. H. Karampelas, Y. H. Kim, and E. P. Furlani, "Photonic and thermofluidic analysis of colloidal plasmonic nanorings and nanotori for pulsed-laser photothermal applications," *J. Phys. Chem. C* **117**(39), 20178–20185 (2013).
  44. A. O. Govorov, W. Zhang, T. Skeini, H. Richardson, J. Lee, and N. A. Kotov, "Gold nanoparticle ensembles as heaters and actuators: Melting and collective plasmon resonances," *Nanoscale Res. Lett.* **1**(1), 84–90 (2006).
  45. D. R. H. C. F. Bohren, *Absorption and Scattering of Light by Small Particles*, 1st ed. (John Wiley & sons, 1983).
  46. A. Rakovich, P. Albella, and S. A. Maier, "Plasmonic control of radiative properties of semiconductor quantum dots coupled to plasmonic ring cavities," *ACS Nano* **9**(3), 2648–2658 (2015).
  47. J. Gargiulo, T. Brick, I. L. Violi, F. C. Herrera, T. Shibanuma, P. Albella, F. G. Requejo, E. Cortés, S. A. Maier, and F. D. Stefani, "Understanding and Reducing Photothermal Forces for the Fabrication of Au Nanoparticle Dimers by Optical Printing," *Nano Lett.* **17**(9), 5747–5755 (2017).
  48. J. Beik, Z. Abed, F. S. Ghoreishi, S. Hosseini-Nami, S. Mehrzadi, A. Shakeri-Zadeh, and S. K. Kamrava, "Nanotechnology in hyperthermia cancer therapy: From fundamental principles to advanced applications," *Journal of Controlled Release* **235**, 205–221 (2016).
  49. L. Carroll and T. R. Humphreys, "LASER-tissue interactions," *Clin. Dermatol.* **24**(1), 2–7 (2006).
  50. V. S. B. C. A. S. Melo, A. L. L. A. Lima, I. R. C. Brasil, O. Castro e Silva Jr, D. V. Magalhães, and L. G. Marcassa, "Characterization of Light Penetration in Rat Tissues," *Journal of Clinical Laser Medicine & Surgery* **19**(4), 175–179 (2001).
  51. A. O. Govorov and H. H. Richardson, "Generating heat with metal nanoparticles," *Nano Today* **2**(1), 30–38 (2007).
  52. H. H. Richardson, M. T. Carlson, P. J. Tandler, P. Hernandez, and A. O. Govorov, "Experimental and theoretical studies of light-to-heat conversion and collective heating effects in metal nanoparticle solutions," *Nano Lett.* **9**(3), 1139–1146 (2009).
  53. S. Li, L. Zhang, X. Chen, T. Wang, Y. Zhao, L. Li, and C. Wang, "Selective Growth Synthesis of Ternary Janus Nanoparticles for Imaging-Guided Synergistic Chemo- and Photothermal Therapy in the Second NIR Window," *ACS Appl. Mater. Interfaces* **10**(28), 24137–24148 (2018).
  54. M. A. Fuller and I. Köper, "Biomedical applications of polyelectrolyte coated spherical gold nanoparticles," *Nano Convergence* **6**(1), 11 (2019).
  55. A. Neely, C. Perry, B. Varisli, A. K. Singh, T. Arbneshi, D. Senapati, J. R. Kalluri, and P. C. Ray, "Ultrasensitive and Highly Selective Detection of Alzheimer's Disease Biomarker Using Two-Photon Rayleigh Scattering Properties of Gold Nanoparticle," *ACS Nano* **3**(9), 2834–2840 (2009).

56. P. Albella, B. Garcia-Cueto, F. González, F. Moreno, P. C. Wu, T. H. Kim, A. Brown, Y. Yang, H. O. Everitt, and G. Videen, "Shape matters: Plasmonic nanoparticle shape enhances interaction with dielectric substrate," *Nano Lett.* **11**(9), 3531–3537 (2011).
57. Z. Liang, W. Liang, W. Shao, J. Huang, T. Guan, P. Wen, G. Cao, and L. Jiang, "Fabrication of tunable aluminum nanodisk arrays: Via a self-assembly nanoparticle template method and their applications for performance enhancement in organic photovoltaics," *J. Mater. Chem. A* **6**(8), 3649–3658 (2018).
58. S. P. Scheeler, D. Lehr, E. B. Kley, and C. Pacholski, "Top-up fabrication of gold nanorings," *Chem. Asian J.* **9**(8), 2072–2076 (2014).
59. S. Behrens, W. Habicht, K. Wagner, and E. Unger, "Assembly of nanoparticle ring structures based on protein templates," *Adv. Mater.* **18**(3), 284–289 (2006).